ANNALS OF GEOPHYSICS, 68, 6, DM690, 2025; doi:10.4401/ag-9429
OPEN ACCESS

Robust Joint Inversion of Gravity and Magnetic Data Using an Lp-Norm Cross-Gradient Strategy in Complex Volcanic Terrains

Indra Arifianto[*,1,2], Kadek Hendrawan Palgunadi[3], Andika Perbawa[4], Jun Nishijima[1]

(1) Earth Resource Engineering Department, Faculty of Engineering, Kyushu University, Fukuoka, Japan
(2) Geological Engineering Department, Faculty of Engineering, Universitas Gadjah Mada, Yogyakarta, Indonesia
(3) Geophysical Engineering Department, Faculty of Civil, Planning, and Geo Engineering, Institute Teknologi Sepuluh Nopember, Surabaya, Indonesia
(4) EXPEC Advanced Research Center, Saudi Aramco, Dhahran, Saudi Arabia

Article history: received September 26, 2025; accepted November 22, 2025

Abstract

In early-stage exploration for minerals, hydrocarbons, and geothermal resources, potential geophysical methods such as Gravity and Geomagnetic surveys stand out for their efficiency, rapid data acquisition, and cost-effectiveness. Despite their advantages, the interpretation of data derived from these methods is often challenged by the non-uniqueness of the solution, leading to potential biases in the subsurface models without the support of additional geological or geophysical data. Our study was initiated by developing forward models based on synthetic gravity and magnetic data configured for volcanic terrains anomaly scenarios. This approach facilitates the evaluation of inversion algorithms to mitigate the inherent non-uniqueness of potential method-derived models. The main objective of our research is to integrate comprehensive regional geological knowledge, which significantly enhances the accuracy of subsurface interpretations when combined with advanced geophysical techniques. This synergy is further exemplified by applying an Lp-Norm fast 3D cross-gradient joint inversion strategy, leveraging gravity and magnetic data to optimize computational efficiency while refining anomaly delineation. Notably, our strategy incorporates a hexahedral terrain model to account for gravitational and magnetic effects of complex terrain, marking a significant advancement in the field. Our findings demonstrate that a nuanced understanding of geological conditions, when integrated with a robust geophysical framework, can lead to the successful reconstruction of volcanic complex subsurface models. This breakthrough has profound implications for geothermal exploration, mineral exploration, and volcanic studies, offering a novel pathway toward more accurate subsurface exploration techniques.

Keywords: Joint Inversion; Gravity; Magnetic; Volcanic Terrain; Cross-Gradient; Lp-Norm

1. Introduction

Exploring Earth's subsurface for mineral, hydrocarbon, and geothermal resources demands efficient and reliable geophysical methods. Among these, gravity and magnetic surveys are widely used during early exploration due to their rapid data acquisition and cost-effectiveness (Telford et al., 1990). However, the interpretation of these datasets is often challenged by the inherent non-uniqueness of potential field inversion, which can yield multiple geologically plausible solutions (Blakely, 1995; Zhdanov et al., 2021; Del Razo Gonzalez and Yutsis, 2023). Reducing this ambiguity requires the integration of additional geological constraints and advanced inversion strategies.

One effective solution is joint inversion, which simultaneously processes multiple geophysical datasets to improve model resolution and reduce ambiguity (Zhdanov et al., 2021). By leveraging the complementary nature of gravity and magnetic data, joint inversion constrains structural geometry more effectively than single-method inversions (Li and Oldenburg, 2000). However, it introduces computational challenges, especially when applied to large or high-resolution datasets, necessitating efficient algorithms and scalable computing (Vatankhah et al., 2020; Liu et al., 2023).

A key aspect of joint inversion is the careful calibration of dataset weighting and regularization parameters. These settings influence how much each dataset contributes to the final model and how geological plausibility is preserved (Zhdanov et al., 2002; Lelièvre and Farquharson, 2013). Advanced techniques such as the cross-gradient method further enhance inversion outcomes by enforcing structural similarity between property models (e.g., density and magnetic susceptibility), improving geological fidelity (Cockett et al., 2015; Zhdanov et al., 2021).

Another important factor is terrain effect. While gravity and magnetic data are typically corrected for topography during preprocessing, complex terrain particularly in volcanic regions must also be considered in forward and inverse modeling to avoid shallow anomaly distortion (Telford et al., 1990; Arifianto et al., 2024). Prior studies (e.g. Blaikie et al., 2014) have demonstrated the importance of incorporating detailed terrain models in potential field modeling, especially for volcanic terrains and similar complex terrains.

In this study, we present an improved joint inversion workflow that integrates a modified hexahedral meshing approach (Arifianto et al., 2024) to efficiently model complex topography. This method is particularly advantageous because the Block Toeplitz with Toeplitz Blocks (BTTB) kernel matrix formulation (Vatankhah et al., 2023) is incompatible with irregular grid geometries. Synthetic gravity and magnetic forward models are constructed to simulate subsurface conditions typical of volcanic terrains. We then apply an Lp-norm-based fast cross-gradient joint inversion approach, supported by an alternating-direction strategy, to address the non-uniqueness of potential field inversion while improving computational efficiency (Vatankhah et al., 2020; Liu et al., 2023). Terrain effects are incorporated directly into the inversion framework, resulting in a more geologically realistic representation of shallow subsurface anomalies.

Our approach emphasizes the integration of geological knowledge to guide inversion and improve interpretation reliability. By combining geophysical modeling, terrain-aware inversion, and geological constraints, we present a robust framework for subsurface characterization in complex volcanic settings. This methodology advances the application of potential field methods in geothermal and mineral exploration and contributes to more accurate and interpretable subsurface models.

2. Methodology

This study adopts a structured methodology to address the inherent non-uniqueness of potential field inversions and to enhance the resolution of subsurface models in volcanic terrains. Successful inversion requires three key inputs: 1) Geophysical data along with associated uncertainties, such as noise levels or standard deviations from data acquisition; 2) Forward modeling equations that define the physical relationship between the subsurface model parameters and the observed data; and 3) Prior geological knowledge, which serves to constrain the solution space and reduce ambiguity which may include geological mapping, petrophysical parameters, or data from drilled wells (Cockett et al., 2015). This study integrates synthetic modeling, advanced inversion algorithms, and geological constraints to achieve robust and geologically meaningful interpretations. The complete workflow is outlined in Fig. 1.

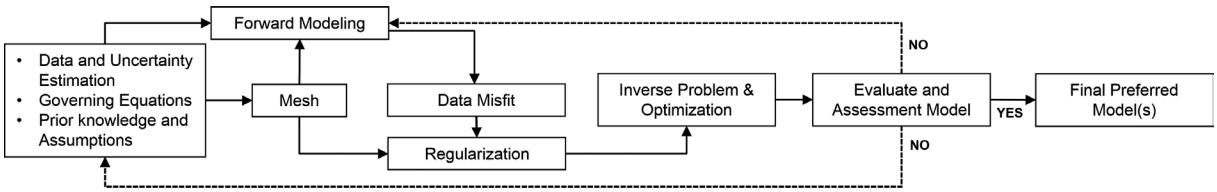

Figure 1. Schematic workflow of the joint inversion process, including topographic mesh generation, forward modeling, inverse problem optimization with regularization, and integration of geological constraints for model evaluation.

2.1 Terrain-Conforming Mesh Construction

The first stage involves generating a topographic mesh using a hexahedral grid technique, designed to conform the complex volcanic terrain surfaces. This technique, based on the approach of Arifianto et al. (2024), ensures accurate surface representation while maintaining computational efficiency. The mesh provides the structural foundation for both gravity and magnetic simulations and accommodates varying topographic gradients often encountered in volcanic regions (Fig. 2). To mitigate edge effects during the inversion process, the model domain is extended by 3 kilometers on each side. This extension ensures that boundary artifacts do not influence the inversion results within the area of interest. All maps and models in this study are referenced to the UTM Zone 49S coordinate system using the WGS 84 datum.

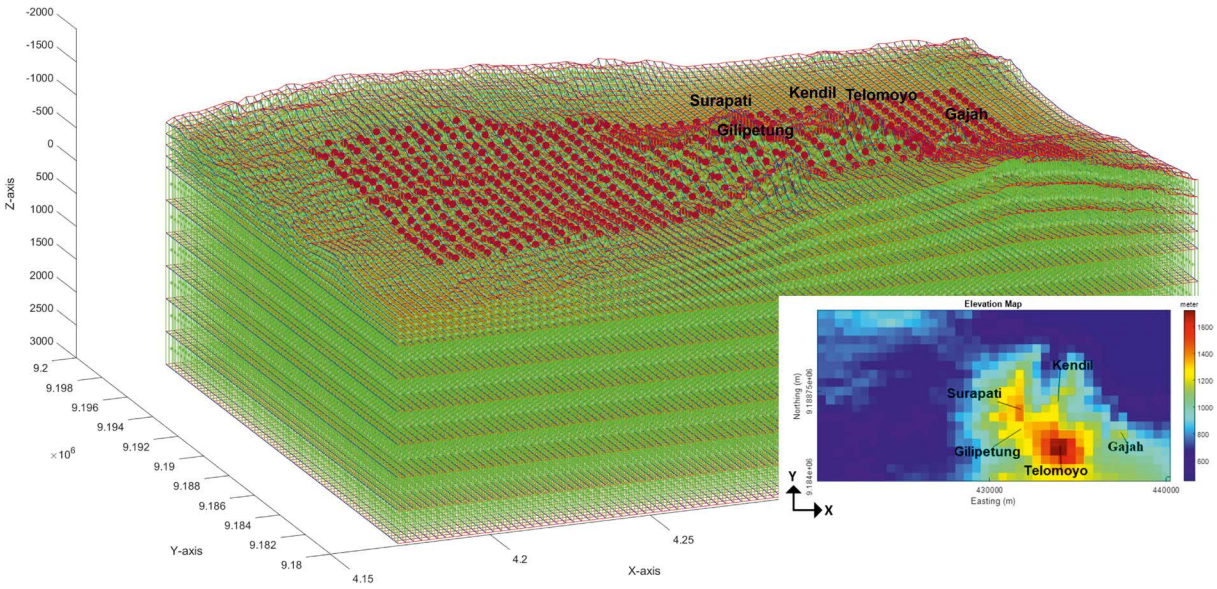

Figure 2. Hexahedral topographic mesh constructed to conform to complex volcanic terrain (red is observation points and green is the central node of density or magnetic susceptibility models). The mesh is constructed based on 250-meter resolution of the DEM data (Arifianto et al., 2024).

2.2 Synthetic Forward Modeling

To assess and validate inversion performance, we construct synthetic model that replicate subsurface geological scenario typical of volcanic environment. The model replicates intrusive bodies, each with predefined density and susceptibility contrasts (Fig. 3). Forward modeling is performed on both gravity and magnetic fields using these synthetic configurations, producing datasets that serve as controlled inputs for inversion testing. Forward modeling for gravity and magnetic is performed based on hexahedral Nagy prism (Plouff, 1976; Nagy et al., 2000; Arifianto et al., 2024).

The synthetic models were constructed to represent four different lithological conditions commonly found in volcanic environments, based on combinations of density and magnetic susceptibility values:

1) High density (+400 kg/m^3) and high magnetic susceptibility (0.05 SI): This configuration represents andesitic to basaltic intrusions with significant magnetite content. It is illustrated by models 3, 6, and 9 (in Fig. 3).
2) High density (+400 kg/m^3) and low magnetic susceptibility (0.001 SI): This case may correspond to altered basaltic intrusions or basaltic bodies with low magnetite concentration, as shown in models 4 and 7.
3) Low density (−300 kg/m^3) and high magnetic susceptibility (0.05 SI): This condition likely represents volcaniclastic deposits or vesicular andesitic-basaltic rocks, which contain abundant magnetic minerals but are relatively porous or fragmented. This is depicted in models 1 and 8.
4) Low density (−300 kg/m^3) and low magnetic susceptibility (0.001 SI): This combination may indicate sedimentary rocks, highly altered volcanic rocks, or volcaniclastic/vesicular andesitic-basaltic materials with minimal magnetite content. This scenario is represented by models 2 and 5.

These four configurations allow us to simulate realistic subsurface heterogeneity in volcanic terrains and evaluate the sensitivity of gravity and magnetic joint inversion to different lithological contrasts.

The forward modeling results show that the Complete Bouguer Anomaly ranges from approximately −1 to 3 mGal, while the Total Magnetic Intensity (TMI) anomaly ranges from around −100 to 1000 nanoTesla (Fig. 3). In this synthetic model, explicit noise due to tools or measurement process was not added to the data. Instead, realistic variability is introduced through the topographic effects, as the observation points are located on an uneven terrain surface. This variation in elevation naturally introduces spatial perturbations that simulate measurement uncertainty and observational noise, particularly relevant in volcanic regions.

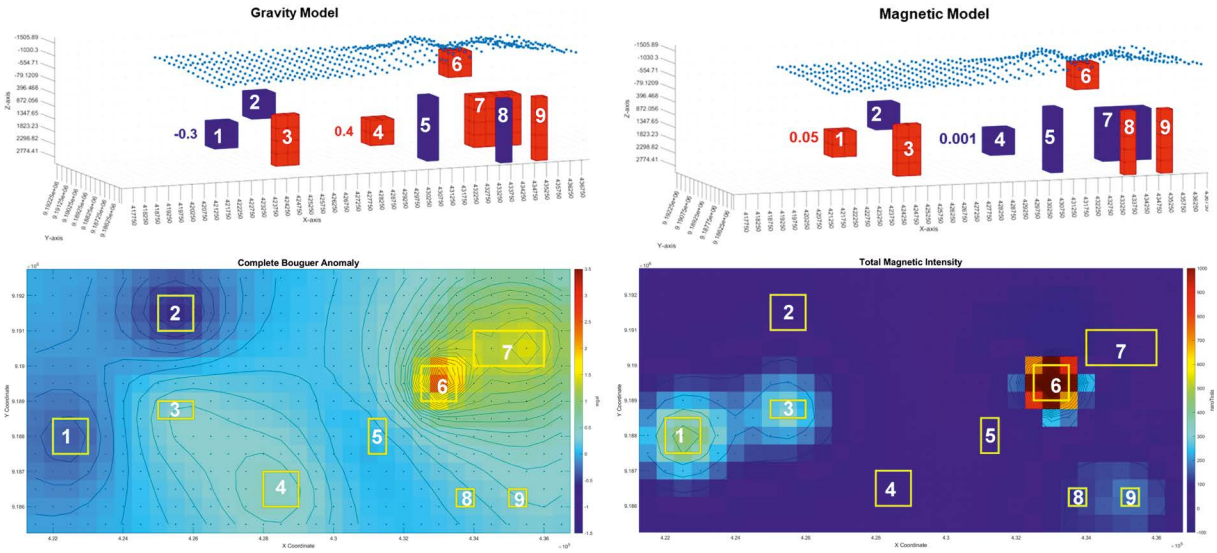

Figure 3. Synthetic subsurface models and their corresponding gravity and magnetic responses (high density and magnetic susceptibility in red color, low density and magnetic susceptibility in blue color), incorporating topography (top panels). The bottom left panel shows the forward-modeled Complete Bouguer Anomaly, and the bottom right panel is forward-modeled Total Magnetic Intensity (yellow rectangle showing the location of each anomalous body).

2.3 Inversion Algorithm Implementation

An alternating-direction Lp-Norm fast 3D cross-gradient joint inversion strategy is incorporated to sequentially optimize each physical property, improving convergence behavior and minimizing unintended coupling between model parameters. Furthermore, this approach also reduces the computational memory required for matrix operations. The core inversion process involves two complementary approaches:

1) Lp-Norm Inversion: Applied separately to gravity and magnetic data to minimize over-smoothing effects and preserve sharp boundaries, especially useful in high-contrast geological settings (Fournier and Oldenburg, 2019; Vatankhah et al., 2023).
2) Fast 3D Cross-Gradient Joint Inversion method: This joint inversion strategy couples gravity and magnetic datasets by enforcing structural similarity through a cross-gradient constraint. To improve computational efficiency, the method adopts a triple sparse matrix format, which stores only the row indices, column indices, and non-zero values of the matrices. This significantly reduces memory requirements and accelerates matrix operations during the inversion process (Liu et al., 2023).

To solve general inversion problem, we need to minimize the global objective function ($\Phi(\boldsymbol{m})$) iteratively at each step ($l = 1,2,3$ ...) (Fournier and Oldenburg, 2019; Vatankhah et al., 2023):

$$\Phi^{(l)}(\boldsymbol{m}) = \left\|\mathbf{W}_d(\boldsymbol{d}^{obs} - \mathbf{G}\boldsymbol{m})\right\|_2^2 + \beta^2\alpha_s\left\|\mathbf{W}_{dh}\mathbf{W}_s^l(\boldsymbol{m} - \boldsymbol{m}^{l-1})\right\|_2^2 + \beta^2 \sum_{j=x,y,z} \alpha_j \left\|\mathbf{W}_{dh}\mathbf{W}_{\mathbf{D}_j}^l\mathbf{D}_j\boldsymbol{m}\right\|_2^2 \quad l = 1,2,3 \ldots \tag{1}$$

Here:
- $\mathbf{W}_d(\boldsymbol{d}^{obs} - \mathbf{G}\boldsymbol{m})$ represents the data misfit term, measuring how well the model $\boldsymbol{m}$ fits the observed data $\boldsymbol{d}^{obs}$ via the forward operator, while $\mathbf{W}_d$ is the data weighting (diagonal matrices of noise or standard deviation of each data point).
- $\mathbf{W}_{dh}\mathbf{W}_s^l(\boldsymbol{m} - \boldsymbol{m}^{l-1})$ is the smallest term, promoting closeness to a reference or prior model $\boldsymbol{m}^{l-1}$, where $\mathbf{W}_{dh}$ is the constant diagonal weighting matrix and $\mathbf{W}_s$ is diagonal smallest weighting.
- $\mathbf{W}_{dh}\mathbf{W}_{\mathbf{D}_j}^l\mathbf{D}_j m$ is the smoothness term, applied along spatial direction $j = x, y, z$, which controls the spatial variability (smoothness or sparsity) of the model. $\mathbf{W_D}$ is the spatial derivative or directional roughness weighting matrix.
- The parameter α_s, α_j and β are trade-off (Lagrange multiplier) parameters that balance the contributions of the data misfit and model regularization terms.

While for the cross gradient joint inversion ($\Phi_{joint}(\boldsymbol{m})$) we need to add the cross-gradient term, so that:

$$\Phi_{joint}(\boldsymbol{m}) = \Phi_1(\boldsymbol{m}) + \Phi_2(\boldsymbol{m}) + \lambda^2\|\boldsymbol{t} + \mathbf{B}(\boldsymbol{m} - \boldsymbol{m}^{apr})\|_2^2 \tag{2}$$

Here:
- $\Phi_1(\boldsymbol{m})$ and $\Phi_2(\boldsymbol{m})$ are the objective functions for the individual gravity and magnetic inversions.
- λ is the trade-off (Lagrange) parameter controlling the strength of the cross-gradient constraint. A smaller value of λ reduces the influence of the cross-gradient term, making the joint inversion resemble two separate single inversions.
- $\boldsymbol{t}$ is the cross-gradient function which quantifies the structural misalignment between the two models, defined as:

$$\boldsymbol{t} = \nabla\boldsymbol{m}_1(x,y,z) \times \nabla\boldsymbol{m}_2(x,y,z) \in \mathcal{R}^{3N} \tag{3}$$

- $\boldsymbol{m}^{apr}$ is the a priori model, which can be defined based on prior geological knowledge or simply set to zero when such information is unavailable
- $\mathbf{B}$ is the Jacobian matrix of discrete approximation for the cross-gradient function, defined as:

$$\mathbf{B} = \begin{pmatrix} \mathbf{B}_{1x} & \mathbf{B}_{2x} \\ \mathbf{B}_{1y} & \mathbf{B}_{2y} \\ \mathbf{B}_{1z} & \mathbf{B}_{2z} \end{pmatrix} \in \mathcal{R}^{3N\times 2N} \tag{4}$$

$$\mathbf{B}_{1x} = \frac{\partial \boldsymbol{t}^x}{\partial \boldsymbol{m}_1}, \mathbf{B}_{1y} = \frac{\partial \boldsymbol{t}^y}{\partial \boldsymbol{m}_1}, \mathbf{B}_{1z} = \frac{\partial \boldsymbol{t}^z}{\partial \boldsymbol{m}_1} \quad \text{and} \quad \mathbf{B}_{2x} = \frac{\partial \boldsymbol{t}^x}{\partial \boldsymbol{m}_2}, \mathbf{B}_{2y} = \frac{\partial \boldsymbol{t}^y}{\partial \boldsymbol{m}_2}, \mathbf{B}_{2z} = \frac{\partial \boldsymbol{t}^z}{\partial \boldsymbol{m}_2} \tag{5}$$

According to Vatankhah et al. (2023), implementing Lp-norm regularization can be approximated by iteratively ($l = 1,2,3$ ...) solving an L2-norm problem with a weighting matrix that depends on the current model. Specifically, the weighting matrices for the model smallness and gradient terms are defined as:

$$\mathbf{W}_S^l = diag\left(((\boldsymbol{m}^l - \boldsymbol{m}^{l-1})^2 + \epsilon_s^2)^{\frac{ps-2}{4}}\right) \tag{6}$$

$$\mathbf{W}_{\mathbf{D}_j}^l = diag\left(\left(\left(\mathbf{D}_j \boldsymbol{m}^l\right)^2 + \epsilon_j^2\right)^{\frac{pj-2}{4}}\right) \quad j = x, y, z. \tag{7}$$

This iterative scheme enables the use of generalized Lp-norms (where $ps, pj \leq 2$) while maintaining the computational advantages of L2-norm formulations (Fournier and Oldenburg, 2019). Although it is possible to use only the smallness term to promote sparsity, Vatankhah et al. (2023) emphasize that combining both smallness and gradient terms under the Lp-norm yields a more robustly sparse solution, especially when inverting complex models or multiple datasets.

To implement the fast 3D joint inversion, we need to store the matrix in a sparse matrix starting from the forward difference matrix $\mathbf{D}_x$, $\mathbf{D}_y$, and $\mathbf{D}_z$ as follow:

$$\mathbf{D}_x = \begin{bmatrix} -1 & 1 & \cdots & 0 \\ 0 & -1 & 1 \cdots & 0 \\ \vdots & \vdots & \ddots & \vdots \\ 0 & 0 & \cdots & 0 \end{bmatrix}_{N\times N} \quad \text{expressed as} \quad \begin{bmatrix} 1 & 1 & -1 \\ 1 & 2 & 1 \\ \vdots & \vdots & \vdots \end{bmatrix}_{2N\times 3}$$

$$\mathbf{D}_y = \begin{bmatrix} -1 & \cdots & 1 & \cdots & 0 \\ 0 & -1 & \cdots & 1 \cdots & 0 \\ \vdots & \vdots & \cdots & \ddots & \vdots \\ 0 & 0 & \cdots & 0 & 0 \end{bmatrix}_{N\times N} \quad \text{expressed as} \quad \begin{bmatrix} 1 & 1 & 1 \\ 1 & 1+Ncol & -1 \\ \vdots & \vdots & \vdots \end{bmatrix}_{2N\times 3}$$

$$\mathbf{D}_z = \begin{bmatrix} -1 & \cdots & \cdots & 1 & \cdots & 0 \\ 0 & -1 & \cdots & \cdots & 1 \cdots & 0 \\ \vdots & \vdots & \cdots & \cdots & \ddots & \vdots \\ 0 & 0 & \cdots & \cdots & 0 & 0 \end{bmatrix}_{N\times N} \quad \text{expressed as} \quad \begin{bmatrix} 1 & 1 & -1 \\ 1 & 1+Nrow\times Ncol & 1 \\ \vdots & \vdots & \vdots \end{bmatrix}_{2N\times 3}$$

This sparse matrix scheme also applied to construct the weighting matrices ($\mathbf{W}_d$, $\mathbf{W}_{dh}$, $\mathbf{W}_s$, $\mathbf{W}_\mathbf{D}$) cross-gradient vector ($\boldsymbol{t}$) and the Jacobian matrices ($\mathbf{B}$) to save the computer memory and computational process (Vatankhah et al., 2023; Liu et al., 2023).

After constructing all the matrices, employing an iterative scheme to update model parameter using solution of linear symmetric positive definite (SPD) system:

$$\mathbf{E}^l \boldsymbol{m}^l = \boldsymbol{f}^l, \quad l = 1,2,3 \ldots \tag{8}$$

The discretization of Eq. (1) and the substitution of Eq. (2) to solve m1 and m2 independently, as described by (Vatankhah et al., 2023) using the following equation:

$$\mathbf{E}_i^l = \mathbf{G}_i^T \mathbf{W}_{d_i^{obs}}^T \mathbf{W}_{d_i^{obs}} \mathbf{G}_i + \lambda_i^2 \left(\mathbf{B}_i^l\right)^T \mathbf{B}_i^l + \beta_i^2 \alpha_s \left(\mathbf{W}_{m_i}^l\right)^T \mathbf{W}_{m_i}^l + \beta_i^2 \sum_{j=x,y,z} \alpha_j \left(\mathbf{W}_{\mathbf{D}_j m_i}^l\right)^T \mathbf{W}_{\mathbf{D}_j m_i}^l \quad i = 1,2 \tag{9}$$

$$\boldsymbol{f}_i^l = \mathbf{G}_i^T \mathbf{W}_{d_i^{obs}}^T \mathbf{W}_{d_i^{obs}} \boldsymbol{d}_i^{obs} + \lambda_i^2 \left(\mathbf{B}_i^l\right)^T \mathbf{B}_i^l \boldsymbol{m}_i^{l-1} - \lambda_i^2 \left(\mathbf{B}_i^l\right)^T \boldsymbol{t}^l + \beta_i^2 \left(\alpha_s \left(\mathbf{W}_{m_i}^l\right)^T \mathbf{W}_{m_i}^l\right) \boldsymbol{m}_i^{l-1} \quad i = 1,2 \tag{10}$$

where $\mathbf{W}_m = \mathbf{W}_{dh}\, \mathbf{W}_s$ and $\mathbf{W}_{\mathrm{D}jm} = \mathbf{W}_{dh} \mathbf{W}_{\mathbf{D}_j} \mathbf{D}_j$. The combined weighting $\mathbf{W}_{dh} = \mathbf{W}_{hard}\, \mathbf{W}_{dept}$ matrix is a diagonal matrix composed of two parts (Vatankhah et al., 2023). The first, $\mathbf{W}_{hard}$, serves to impose hard constraints on specific

model parameters. If certain model values are known in advance such as from borehole data or geological surveys the corresponding diagonal elements in $\mathbf{W}_{hard}$ are set to large values to enforce these known conditions, and those positions in the model vector are fixed to the known values. For unknown parameters, the diagonal entries are simply set to 1. This ensures that known values remain unchanged during the inversion iterations. The second component, $\mathbf{W}_{dept}$, is a depth-based weighting function expressed as $(\boldsymbol{z} + z_{av})^{-v/2}$, where z represents the depth of each model cell and v is a tunable parameter (Li and Oldenburg, 2000). This weighting is designed to compensate for the natural decrease in sensitivity of the geophysical kernel functions with increasing depth.

The strategy for selecting an appropriate regularization parameter and defining a stopping criterion for the alternating direction regularized inverse problem is known as the cooling-warming strategy. In this approach, the Lagrange multiplier (β) is dynamically adjusted based on how close the current data misfit is to the target threshold. This threshold is determined using the discrepancy principle (Vatankhah et al., 2023), which ensures that the misfit does not exceed the expected noise level in the observed data. Convergence is achieved when the data misfit satisfies:

$$\left\|(\boldsymbol{d}_i^{obs} - \mathbf{G}_i\boldsymbol{m}_i)\right\|_2^2 \leq N_i \cdot \sigma_i^2 \quad \text{for } i = 1,2 \tag{11}$$

Here N is the number of observations and σ^2 is the variance of data noise. To reach this criterion, the cooling-warming strategy adjusts the regularization parameter β iteratively using the rule:

$$\beta_i^{l+1} = \begin{cases} \beta_i^{l-1}/(q_i \times 1.1), & if \quad \left\|(\boldsymbol{d}^{obs} - \mathbf{G}\boldsymbol{m})\right\|_2^2 \leq N \cdot \sigma^2 \\ \beta_i^l . q_i & Otherwise \end{cases} \quad \text{for } i = 1,2 \tag{12}$$

Where $0 < q_i < 1$ is a decay factor. When the misfit is below the noise threshold, the method cools (lower β value), allowing the inversion to better fit data and reveal finer structures. When the misfit is above the noise threshold, the method warms (higher β value) to enforce stronger model regularization to stabilize the inversion.

2.4 Integration of Geological Constraints

Regional geological information such as surface mapping, stratigraphic profiles, and lithological sample data is integrated into the inversion framework as geological constraints. These constraints help steer the inversion toward solutions that are not only mathematically stable but also geologically realistic. By incorporating this prior knowledge or a priori model if available ($\boldsymbol{m}^{apr}$, $\mathbf{W}_{hard}$), we significantly reduce solution ambiguity and ensure better alignment between the model outputs and known subsurface features (Cockett et al., 2015).

Additionally, regularization parameters including depth weighting functions ($\mathbf{W}_d$, $\mathbf{W}_{dh}$, $\mathbf{W}_s$, $\mathbf{W}_D$), and upper (ub) and lower bounds (lb) for density or magnetic susceptibility (ρ_{min}, ρ_{max}, κ_{min}, κ_{max}) are carefully adjusted based on the specific geological conditions of the study area (Eq. 13). The inversion process is iteratively refined using these constraints to enhance model fidelity and improve structural accuracy (Fig. 4).

$$m_i = \begin{cases} lb_i, & m_i < lb_i \\ m_i, & lb_i \leq m_i \leq ub_i \\ ub_i, & m_i < ub_i \end{cases} \quad \text{for } i = 1,2 \tag{13}$$

Input: Data vector $\boldsymbol{d}_i^{obs}$ and matrices data variance $\mathbf{W}_{d_i^{obs}}$ (if available or set =1)
Prior information: vector model ($\boldsymbol{m}_i^{apr}$) (if available or set =0) and $\mathbf{W}_{hard\ i}$ (set=1).
Bound constrains: $\rho_{min}, \rho_{max}, \kappa_{min}, \kappa_{max}$
Meshing and function to calculate operation matrices $\mathbf{G}_i$, $\mathbf{D}_j$ for $i = 1,2$ and $j = x, y, z$
Parameters: $\epsilon_s, \epsilon_j, p_s, p_j, v_i, \alpha_s, \alpha_j, \beta_i, \lambda_i$ and q_i for $i = 1,2$ and $j = x, y, z$
Set maximum number of iterations L_{max}
Calculate $\mathbf{W}_{dh\ i}$
Set $l = 0$
Initialize $\boldsymbol{m}_i^l = \boldsymbol{m}_i^{apr}$, $\mathbf{W}_{s\ i}^l$ and $\mathbf{W}_{\mathbf{D}\ ji}^l$ as $Identity\ matrix\ N \times N$ for $i = 1,2$ and $j = x, y, z$
while not converged, $\left\|(\boldsymbol{d}^{obs} - \mathbf{G}\boldsymbol{m})\right\|_2^2 \leq N \cdot \sigma^2$ for both data not satisfied, and $l < L_{max}$
  $l = l + 1$
  Compute $\boldsymbol{t}^l$, $\mathbf{B}_1^l$, $\mathbf{E}_1^l$ and $\boldsymbol{f}_1^l$
  Solve m_1^l using preconditioned conjugate gradient (*pcg* function in MATLAB);
  Impose constraint $\rho_{min} \leq \boldsymbol{m}_1^l \leq \rho_{max}$
  Update $\boldsymbol{t}^l$ and $\mathbf{B}_2^l$ using $\boldsymbol{m}_1^l$ and compute $\mathbf{E}_2^l$ and $\boldsymbol{f}_2^l$
  Solve $\boldsymbol{m}_2^l$ using preconditioned conjugate gradient
  Impose constraint $\kappa_{min} \leq \boldsymbol{m}_2^l \leq \kappa_{max}$
  Test convergent criteria $\left\|(\boldsymbol{d}^{obs} - \mathbf{G}\boldsymbol{m})\right\|_2^2 \leq N \cdot \sigma^2$ stop loop if both converge
  If $\left\|(\boldsymbol{d}^{obs} - \mathbf{G}\boldsymbol{m})\right\|_2^2 \leq N \cdot \sigma^2$, set $\beta_i^l = \beta_i^{l-1} / (q_i \times 1.1)$ else $\beta_i^l = \beta_i^{l-1}\ q_i$ for $i = 1,2$
  Update $\mathbf{W}_{s\ i}^l$ and $\mathbf{W}_{\mathbf{D}\ ji}^l$ for $i = 1,2$ and $j = x, y, z$ (Eq 5 and 6)
end while
Output: model vector $\boldsymbol{\rho} = \boldsymbol{m}_1^l$ and $\boldsymbol{\kappa} = \boldsymbol{m}_2^l$

Figure 4. Simplified algorithm of the joint inversion process using Lp-norm regularization and an alternating-direction strategy with adaptive parameter tuning (modified after Vatankhah et al., 2023).

2.5 Model Evaluation and Interpretation

The inversion results were evaluated by comparing the reconstructed anomalies against the known synthetic model. Several criteria were used to assess model performance, including the data misfit, structural correspondence, and the clarity of anomaly boundary delineation. A well-regularized inversion is indicated by a progressive reduction in data misfit norm ($\left\|\boldsymbol{d}^{obs} - \mathbf{G}\boldsymbol{m}\right\|_2^2$) across iterations and a corresponding decrease in the model norm ($\|\boldsymbol{m}\|_2^2$) (Fig. 5a). This behavior reflects an appropriate balance between fitting the observed data and maintaining a geologically reasonable model, governed by the choice of weighting parameters that determine the minimization of the objective function in Eq. (1). The inversion result is accepted when the data misfit meets the discrepancy criterion in Eq. (11), or when further iterations produce only marginal reductions in the misfit and the model (density or magnetic susceptibility) stabilizes, indicated by a sufficiently small rate of change in the model contrast.

In cases where the input data exhibit low variance, the inversion is expected to yield a low misfit. However, excessively low misfit values may indicate overfitting, especially in the presence of noise. Overfitting occurs when the model attempts to explain noise rather than true subsurface structure, resulting in unrealistic or unstable solutions. To detect such modeling errors, we analyze the spatial distribution of residuals, visualized through data misfit maps (Fig. 5b). These maps help identify regions where the inversion struggles to match the observed data, which may correspond to zones of modeling uncertainty, insufficient resolution, or high noise levels. Therefore, the misfit map serves as a diagnostic tool to evaluate local model reliability and guide interpretation refinement.

Last criteria of the inversion results, structural correspondence and clarity of anomaly boundaries, are evaluated using the cross-gradient magnitude (Eq. 3), together with the model gradient amplitude ($\|\nabla \boldsymbol{m}(x, y, z)\|$). These diagnostic measures are illustrated by the model cross-sections provided in the Results and Discussion section.

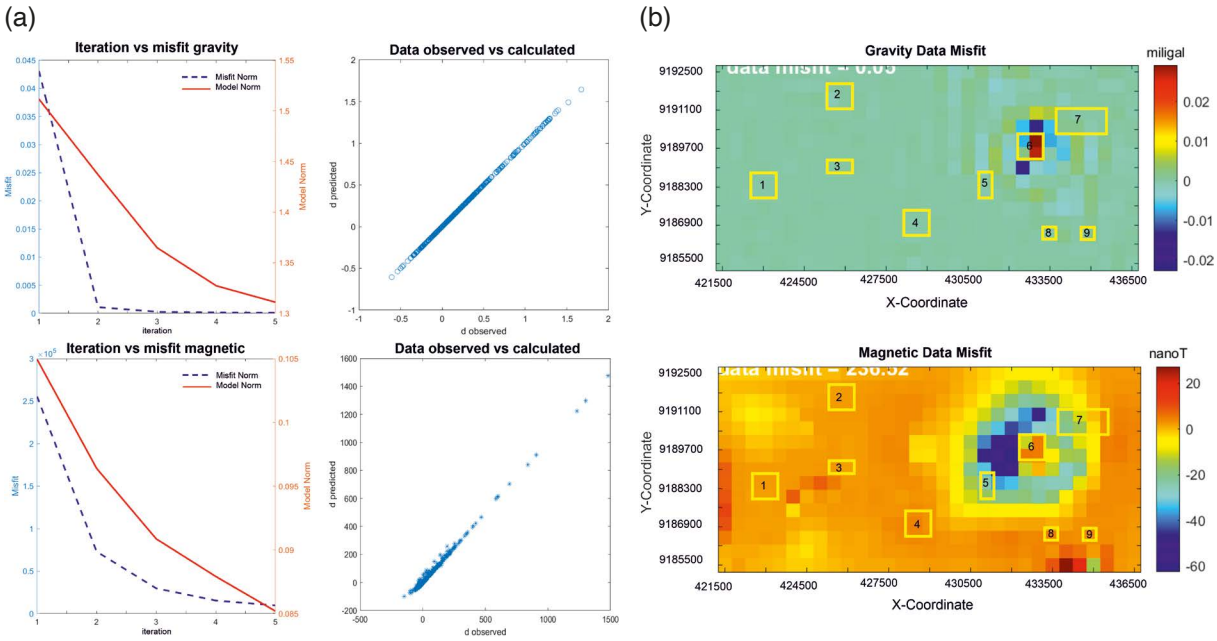

Figure 5. Model evaluation results showing joint inversion performance. (a) Misfit reduction over iterations and comparison of observed vs. calculated data for gravity (top) and magnetic (bottom) datasets. (b) Final spatial distribution of gravity and magnetic data misfits, used to assess model accuracy and fit quality.

3. Result and Discussion

3.1 Joint Inversion of synthetic model of Volcanic Terrain

The inversion was performed using both single-method approaches of gravity and magnetic data implemented with the same weighting parameter and assumption via commercial software, as well as a joint inversion algorithm developed in MATLAB. For visualization, 3D rendering was conducted using Voxler software, which offers enhanced volume representation of subsurface models.

In the single inversion results, significant ambiguities were observed, especially in the vertical and lateral extents of the anomalies due to the inherent non-uniqueness of potential field methods. The gravity single inversion failed to detect anomalies 8 and 9, likely due to their low-density contrast or spatial overlap with stronger nearby anomalies (Fig. 6a). In the magnetic single inversion, anomalies 2, 4, and 7 were not adequately recovered due to their low magnetic susceptibility contrasts (Fig. 6b). Even anomaly 3, despite having a higher susceptibility, was poorly resolved, indicating the limited depth sensitivity of magnetic inversion in the absence of additional structural constraints. Furthermore, anomaly 5, which was modeled with low susceptibility, was incorrectly reconstructed as a high-susceptibility zone likely due to interference effects or overfitting of the data misfit (Fig. 6b).

In contrast, the joint inversion using the Lp-norm and cross-gradient constraint substantially improved the reconstruction of subsurface structures. The joint model was able to resolve both high-density and low-density bodies more effectively. However, anomalies 8 and 9 were only partially recovered, with their upper portions detected but not extending to the full intended depth (Fig. 6c). Similarly, anomaly 5 appeared overly diffused around anomaly 6, suggesting some level of spatial smearing. These limitations were reflected in the gravity data misfit map, which showed misfit error reaching ±0.02 mGal (Fig. 5b). The magnetic data misfit exhibited a similar pattern which has high error around anomaly 6 (Fig. 5b). In the magnetic joint inversion, only anomalies with high magnetic susceptibility (models 1, 3, 6, 8, and 9) were accurately resolved (Fig. 6d). The inability to recover low-susceptibility anomalies, such as models 2, 4, and 7, may be attributed to their low signal amplitudes, which were likely masked by stronger nearby sources or terrain-induced noise effects.

It is clear that inclusion of the cross-gradient term effectively enforced structural similarity between the density and susceptibility models, improving the spatial alignment of geological boundaries. The use of an alternating-direction inversion strategy contributed to improved convergence stability and suppressed property coupling

between density and susceptibility models. Moreover, the cooling-warming regularization scheme allowed for dynamic adjustment of the Lagrange multipliers, balancing data fidelity with model smoothness throughout the inversion process.

Importantly, terrain effects were incorporated directly through the use of a hexahedral mesh, enabling the model to preserve the true topographic geometry. This approach allowed for more realistic reconstruction of shallow anomalies, especially in areas of rugged volcanic terrain. Overall, the final joint inversion model showed a high degree of agreement with the synthetic model, demonstrating the method's robustness and suitability for resolving geologically complex subsurface structures in volcanic settings.

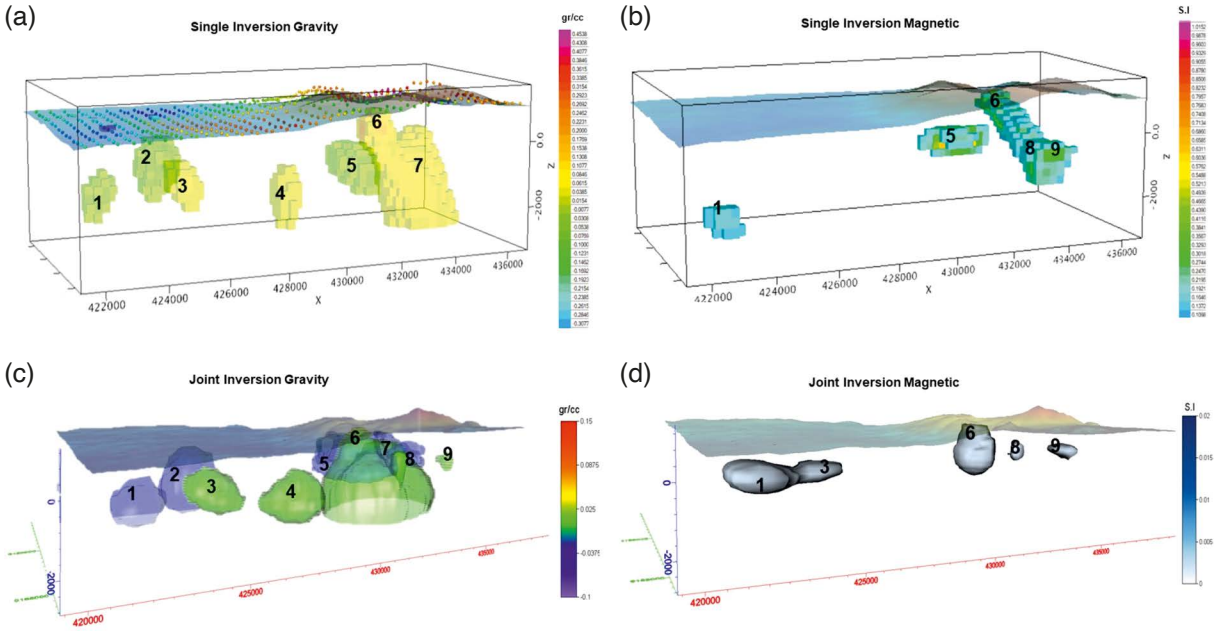

Figure 6. Comparison of 3D inversion results from single-method and joint inversion approaches. (a) Gravity-only inversion showing partial recovery of anomalies 1-7. (b) Magnetic-only inversion, with limited detection of anomalies 1 and 5-9. (c) Joint inversion results for density distribution, showing improved reconstruction of anomalies 1-9. (d) Joint inversion results for magnetic susceptibility, highlighting better structural alignment of high-susceptibility anomalies (e.g. 6, 8, and 9) and improved model consistency.

3.2 Joint Inversion of Real Data in Telomoyo Mountain Area

The proposed method was next applied to real gravity and magnetic datasets acquired from the Telomoyo Mountain geothermal prospect in Central Java, Indonesia. The region is characterized by a volcanic complex with significant topographic relief and has potential of 55 MW geothermal resources (Umam et al., 2020), making it a suitable place for geothermal exploration using gravity and magnetic the inversion framework.

Gravity data were corrected for terrain correction using MAETEC to obtain the Complete Bouguer Anomaly (Arifianto et al., 2025). Magnetic data were reduced to the pole (RTP), and both gravity and magnetic fields were residualized using wavelength-based filtering guided by spectral inspection to emphasize near-surface sources (Fig. 7). The grid employs a hexahedral mesh that conforms to rugged terrain (Fig. 2), minimizing topography-related modeling bias.

Geological priors were imposed as bounds on property contrasts. For density, we used a background of 2530 kg/m^3 with bounds −400 to +500 kg/m^3 relative to background (consistent with sedimentary to andesitic-basaltic ranges). For magnetic susceptibility, we applied bounds from -1×10^{-4} SI to 0.1 SI. The upper bound reflects typical induced susceptibilities for most crustal rocks, while the small negative lower bound accounts for diamagnetic materials, common in sedimentary lithologies. Allowing negative values is compatible with the induced-magnetization assumption in reduced-to-pole (RTP) modeling and is particularly relevant when modeling diamagnetic or weakly

magnetic units. Larger negative values or arbitrary directions are generally reserved for full vector-magnetization inversions.

The gravity misfit map shows localized residuals in the crater area with amplitudes on the order of ±0.1 mGal, indicating slight under- or overestimation of density contrast, particularly in parts of the crater where the terrain is steep and shallow subsurface properties vary sharply (Fig. 7a). The magnetic misfit map is near-zero over most of the area but exhibits a pronounced negative residual (−500 nT) in the eastern sector (Fig. 7b). This pattern is consistent with (i) low-susceptibility targets masked by stronger nearby sources, (ii) imperfect RTP parameters (inclination/declination) or unmodeled remanent magnetization, and/or (iii) discretization limits near steep topography.

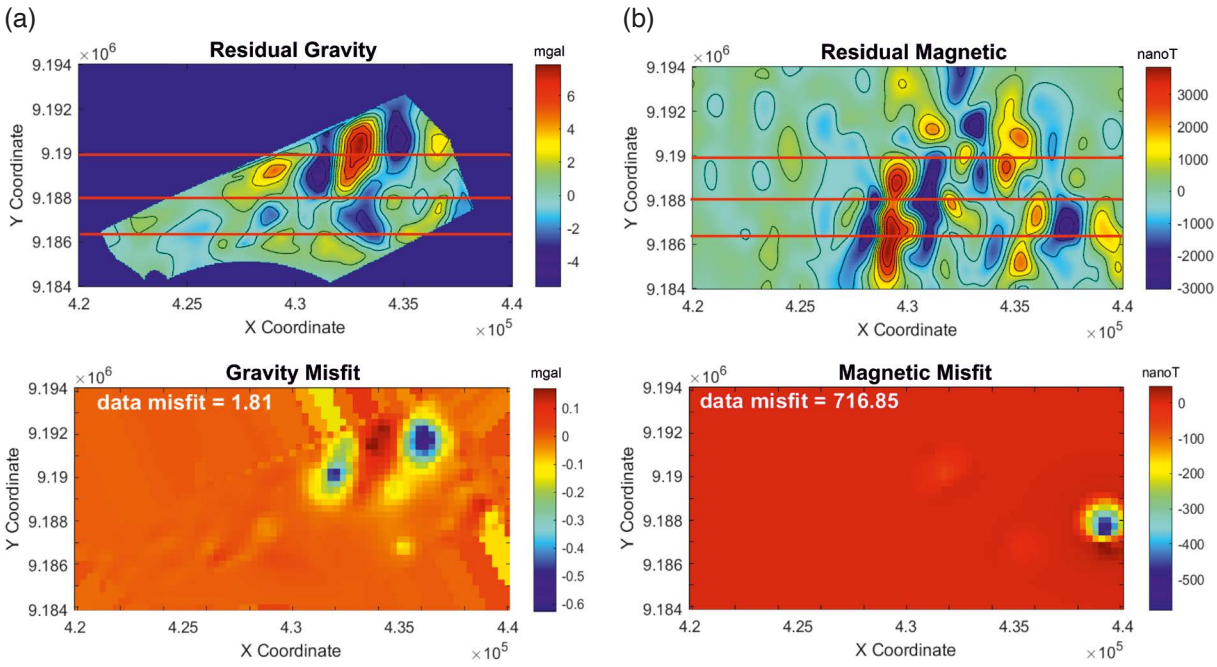

Figure 7. Residual and misfit maps for gravity (a) and magnetic (b) data. Top panels show residual anomalies after regional-residual separation (red lines shows section location in the Figs. 8 and 9). Bottom panels display spatial distribution of data misfits, with total misfit values of 1.81 mGal for gravity and 716.85 nT for magnetics.

To evaluate the inversion model results, we compare three sections across Y-coordinates of 9,190,000; 9,188,000; and 9,186,500 of single and joint inversion. Overall, the joint gravity-magnetic inversion sharpens contacts and improves vertical continuity relative to the single inversions, with fewer topography-related artifacts.

In the line 9,190,000 (Fig. 8a), A compact high-density rocks (>2620 kg/m^3) occurs beneath the high positive gravity anomaly in the crater-like area (see Fig. 7a), consistent with a high density (~2700 kg/m^3) andesitic-basaltic intrusion in CTL-1 and CTL-2 wells (Hermawan et al., 2016a; Hermawan et al., 2016b). Surrounded by the low-density area (<2400 kg/m^3) interpreted as the product of volcaniclastic/vesicular deposits forming the Kendil, and Surapati cones. In the line 9,188,000 (Gilipetung area), The joint inversion model resolves several moderate density highs (~2550-2620 kg/m^3) separated by lower-density lenses, compatible with stacked intrusions or dike swarms emplaced into a pyroclastic pile (Fig. 8a). Lastly in the line 9,186,500 (around Telomoyo summit), A steep dense plug in the east part under Mt. Telomoyo is bordered to the west flank by a low-density wedge, interpreted as alteration or volcanic lahar deposits (Fig. 8a).

In parallel with the density results, the joint inversion resolves magnetic susceptibility more clearly than the single inversion. The single inversion exhibits spotty, high-amplitude spikes and occasional non-physical negative magnetic susceptibility, whereas the joint inversion yields a spatially coherent magnetic susceptibility structure that aligns with the density model and regional geology. Notably, high magnetic susceptibility anomalies (>10^{-3} SI) define a north-south trend along the volcanic edifice or regional structure alignment, consistent with fresh lavas and/or magnetite-bearing intrusions (high magnetic anomaly) beneath the Gilipetung and Kendil volcanic cones (Fig. 7b).

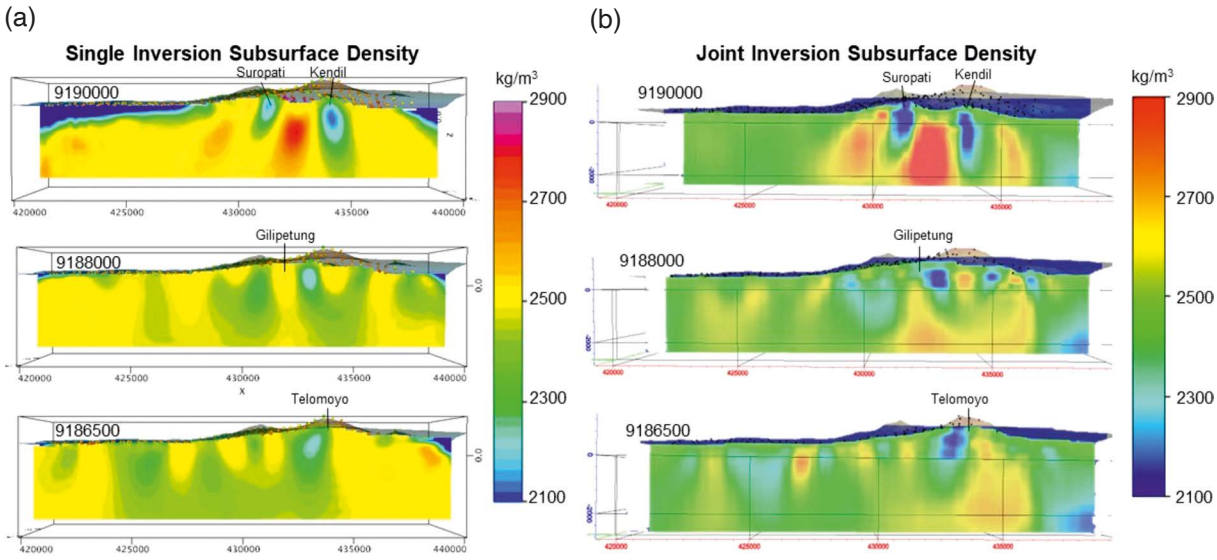

Figure 8. Comparison of 2D cross-sections from gravity single inversion (a) and joint gravity-magnetic inversion (b) results along Y-coordinates 9,190,000; 9,188,000; and 9,186,500. Joint inversion better delineates high- and low-density structures with clearer vertical continuity and reduced ambiguity.

Around the older intrusion body imaged by density (crater-like area), magnetic susceptibility is systematically lower, which is compatible with hydrothermal alteration or demagnetization consistent with the CTL-1 and CTL-2 wells that report intense alteration (Annisa et al., 2019).

Along line 9,190,000, the single inversion produces spotty, high-amplitude magnetic susceptibility spikes, while the joint inversion resolves a coherent positive magnetic susceptibility band (up to ~0.1 SI) flanking the dense core and a lower-magnetic susceptibility cap near the surface. This pattern is consistent with a magnetite-rich intrusion overlain by altered or vesicular cover. The negative magnetic susceptibility patches seen in the single inversion are non-physical under induced-field RTP assumptions and likely reflect unmodeled remanent magnetization or insufficient constraints (Fig. 9a).

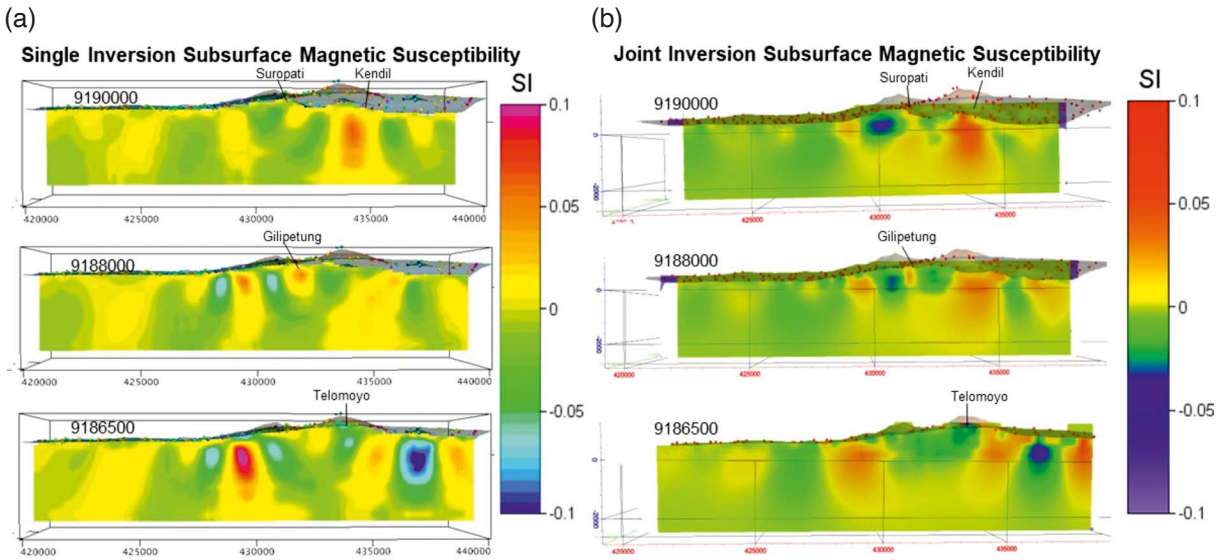

Figure 9. Subsurface magnetic susceptibility (SI) sections from magnetic single inversion (a) and joint gravity-magnetic inversion (b) along Y-coordinates 9,190,000; 9,188,000; and 9,186,500. The joint inversion suppresses artifacts and yields more coherent magnetic susceptibility structure, better separating high-magnetic susceptibility intrusions from low magnetic susceptibility altered or volcaniclastic units.

For line 9,188,000 (Gilipetung area), the single inversion alternates blue-orange lobes that appear as oscillatory artifacts (Fig. 9a). In contrast, the joint inversion co-locates moderate magnetic susceptibility highs with the density highs, indicating magnetite-bearing intrusions, while the intervening lower magnetic susceptibility lenses likely mark hydrothermal alteration and/or oxidation of titanomagnetite (magnetite into hematite) within the pyroclastic sequence (Fig. 9b). Lastly in the line 9,186,500 (around Telomoyo summit), the joint inversion shows a localized negative magnetic susceptibility zone on the east of Telomoyo mountain. These features mirror the density low and correspond to the eastern magnetic misfit concentration noted earlier, pointing to low-susceptibility lithology and/or remanent magnetization (Fig. 9b).

The joint inversion, using Lp-norm regularization and cross-gradient coupling, provided a more coherent subsurface model, with structurally consistent features observed in both density and susceptibility distributions. Notably, the joint model delineated a possible low-density, high-susceptibility zone that may represent a hydrothermally altered volcanic conduit or fractured reservoir zone. Incorporating terrain effects directly into the forward and inversion process proved essential, especially in resolving shallow features near steep slopes. The improved imaging of near-surface anomalies contributes to a better understanding of potential geothermal pathways and supports more informed exploration targeting.

4. Conclusions

This study demonstrates a joint gravity-magnetic inversion workflow tailored for volcanic terrains that (i) builds a terrain-conforming hexahedral mesh to honor rugged topography, (ii) couples datasets with an Lp-norm, cross-gradient formulation solved by an alternating-direction strategy, and (iii) improves efficiency using triple sparse matrices storage and a cooling-warming scheme for adaptive regularization. Synthetic tests spanning high/low density-susceptibility combinations demonstrated that the joint formulation systematically sharpens contacts, reduces lateral smearing, and improves vertical continuity relative to single-method inversions.

Applied to Telomoyo volcanic complex, the joint inversion resolves a compact high-density core (>2620 kg/m^3) beneath the crater-like feature, consistent with magnetite-bearing andesitic-basaltic intrusion, flanked by low-density rocks (<2400 kg/m^3) interpreted as volcaniclastic deposits. Magnetic susceptibility results reveal a coherent north-south chain of high magnetic susceptibility anomalies (>10^{-3} SI) following volcanic edifices, suggesting fresh lava or intrusion zones, while low magnetic susceptibility model around the central intrusion match alteration zones confirmed by well data. Misfit analysis indicate that the remaining discrepancies are localized within topographically complex sectors in the gravity data and within an eastern magnetic residual, which is more likely attributable to remanent magnetization or mismatches in RTP parameters than to systematic model bias.

These results illustrate how simultaneously inverting gravity and magnetic observations exploits the different sensitivities of the two datasets to produce a single, geologically consistent model. This integrated approach sharpens contacts, improves vertical continuity, and reliably identifies alteration zones and intrusive bodies, critical features for geothermal targeting in complex volcanic systems.

Data availability statement. Share upon reasonable request for MATLAB code and data sharing policy.

Acknowledgements. This research was supported by the Japan International Cooperation Agency (JICA) through the provision of a scholarship and research funding, for which the author expresses sincere gratitude. The authors also acknowledge the valuable contributions and constructive discussions from colleagues at the Geothermic Laboratory, Department of Earth Resource Engineering, Kyushu University. Appreciation is extended to PT Geo Dipa Energy for granting permission to use their gravity data in this research, and to the reviewers for their constructive feedback that greatly improved the quality of this manuscript.

References

Annisa, H. U., H. Niniek Rina and D. Hermawan (2019). Fluid evolution of Umbul-Telomoyo Geothermal system, IOP Conf. Ser., Earth Environ. Sci., 254, 012003, doi:10.1088/1755-1315/254/1/012003.

Arifianto, I., J. Nishijima and A. Darmawan (2024). Terrain Effects on Gravity and Magnetic Responses: Insights from Forward Modeling in Telomoyo Geothermal Exploration Area, in Proceeding of International Symposium on Earth Science and Technology 2024, CINEST, Fukuoka, 496-501.

Arifianto, I., R. C. Wibowo and J. Nishijima (2025). MAETEC: An Optimized MATLAB-Based Approach for Accurate and Efficient Terrain Correction in Complete Bouguer Anomaly, RGN Zbornik, 5, 76, doi:10.17794/rgn.2025.5.4.

Blaikie, T. N., L. Ailleres, P. G. Betts and R. A. F. Cas (2014). Interpreting subsurface volcanic structures using geologically constrained 3-D gravity inversions: Examples of maar-diatremes, Newer Volcanics Province, southeastern Australia, J. Geophys. Res., Solid Earth, 119, 4, 3857-3878, doi:10.1002/2013JB010751.

Blakely, R. J. (1995). Potential theory in gravity and magnetic applications, Cambridge University Press, Cambridge, England, New York.

Cockett, R. S., L. J. Kang, A. Heagy, A. Pidlisecky et al. (2015). SimPEG: An open-source framework for simulation and gradient based parameter estimation in geophysical applications, Comput. Geosci., 85, 142-154, doi:10.1016/j.cageo.2015.09.015.

Del Razo Gonzalez, A. and V. Yutsis (2023). Robust 3D Joint Inversion of Gravity and Magnetic Data: A High-Performance Computing Approach, Appl. Sci., 13, 20, 11292, doi:10.3390/app132011292.

Fournier, D. and D. W. Oldenburg (2019). Inversion using spatially variable mixed ℓp norms, Geophys. J. Int., 218, 1, 268-282, doi:10.1093/gji/ggz156.

Hermawan, D., D. I. Setiawan and E. Suhanto (2016a). Landaian Suhu Sumur CTL-1 Daerah Panas Bumi Candi Umbul-Telomoyo Kabupaten Semarang, Provinsi Jawa Tengah, in Hasil Kegiatan Lapangan Tahun 2016 Pusat Sumber Daya Mineral, Batubara dan Panas Bumi, Badan Geologi, Kementrian ESDM, 327.

Hermawan, D., D. I. Setiawan and E. Suhanto (2016b). Landaian Suhu Sumur CTL-2 Daerah Panas Bumi Candi Umbul-Telomoyo Kabupaten Semarang, Provinsi Jawa Tengah, in Hasil Kegiatan Lapangan Tahun 2016 Pusat Sumber Daya Mineral, Batubara dan Panas Bumi, Badan Geologi, Kementrian ESDM, 473.

Lelièvre, P. G. and C. G. Farquharson(2013). Gradient and smoothness regularization operators for geophysical inversion on unstructured meshes, Geophys. J. Int., 195, 1, 330-341, doi:10.1093/gji/ggt255.

Li, Y. and D. W. Oldenburg (2000). Joint inversion of surface and three-component borehole magnetic data, Geophysics, 65, 2, 540-552, doi:10.1190/1.1444749.

Liu, S., X. Wan, S. Jin, B. Jia et al. (2023). Fast 3D joint inversion of gravity and magnetic data based on cross gradient constraint, J. Geodyn., 14, 4, 331-346, doi:10.1016/j.geog.2022.12.003.

Nagy, D., G. Papp and J. Benedek (2000). The gravitational potential and its derivatives for the prism, J. Geod., 74, 7-8, 552-560, doi:10.1007/s001900000116.

Plouff, D. (1976). Gravity And Magnetic Fields of Polygonal Prisms and Application to Magnetic Terrain Corrections, Geophysics, 41, 4, 727-741, doi:10.1190/1.1440645.

Telford, W. M., L. P. Geldart and R. E. Sheriff (1990). Applied Geophysics, 2nd ed., Cambridge University Press.

Umam, M. F., J. Susilo, D. P. Purba and D. W. Adityatama (2020). Design of Geothermal Drilling Training Curriculum as the Implementation of the National Competence Standard on Onshore Drilling, IOP Conference Series, Earth. Environ. Sci., 417, 1, 012016, doi:10.1088/1755-1315/417/1/012016.

Vatankhah, S., X. Huang, R. A. Renaut, K. Mickus et al. (2023). Efficiently Implementing and Balancing the Mixed Lp-Norm Joint Inversion of Gravity and Magnetic Data, IEEE Trans. Geosci. Rem. Sens., 61, 1-17, doi:10.1109/TGRS.2023.3292889.

Vatankhah, S., S. Liu, R. A. Renaut, X. Hu et al. (2020). An Efficient Alternating Algorithm for the Lp-Norm Cross-Gradient Joint Inversion of Gravity and Magnetic Data Using the 2-D Fast Fourier Transform, IEEE Trans. Geosci. Rem. Sens., 60, 1-16, doi:10.1109/TGRS.2020.3033043.

Zhdanov, M. S., R. G. Eliss, S. Mukherjee and D. Pavlov (2002). Regularized Focusing Inversion of 3-D Gravity Tensor Data, Presented at the 2002 SEG Annual Meeting, Salt Lake City, Utah, October 2002, SEG-2002-0751.

Zhdanov, M. S., M. Jorgensen and L. Cox (2021). Advanced Methods of Joint Inversion of Multiphysics Data for Mineral Exploration, Geosciences, 11, 6, 262, doi:10.3390/geosciences11060262.

***CORRESPONDING AUTHOR: Indra ARIFIANTO**,
Earth Resources Engineering, Faculty of Engineering, Kyushu University, Fukuoka, Japan
e-mail: indra.arifianto@mail.ugm.ac.id